ORIGINAL ARTICLE

A novel framework using FEM and machine learning models with experimental verification for Inconel-718 rapid part qualification by laser powder bed fusion

Muhammad Arif Mahmood[1] · Usman Tariq[2]

Abstract

This study establishes a novel printability criterion for Inconel-718 parts by laser power bed fusion. For this purpose, the regions with $D/t \leq 1.15$, $L/W > 2.1$, and $W/D = 2.0$ have been identified with lack-of-fusion, balling, and keyhole defects. Regimes within the processing maps related with defects have been regarded as a melt pool geometry function, derived using a FEM model with temperature-dependent thermophysical properties. The data was collected, via design of experiment technique, using validated simulation model. Following that, the acquired data was utilized to train and test a machine learning model based on a backpropagation artificial neural network (ANN). By linking melt pool dimensional ratios to defects, the validated ANN model was used to produce processing maps. The processing maps were validated using experimental analyses, which revealed a consistent correlation between experiments and simulations. The proposed processing maps can be utilized to quickly quantify the Inconel-718 parts generated by the LPBF.

Keywords Laser powder bed fusion · Inconel-718 · Processing maps · Defect identification · Rapid part qualification

1 Introduction

Additive manufacturing (AM) refers to the process of creating objects from 3D model data by progressively joining materials, typically layer by layer [1]. AM is also known as rapid manufacturing or rapid prototyping [2]. Unlike conventional manufacturing methods that involves material removal from a larger stock to fabricate products, AM constructs the final shape by adding materials [3–5]. This approach optimizes raw material utilization, minimizes waste production, and achieves precise geometric accuracy [6, 7]. Utilizing AM, a computerized 3D solid model can be directly transformed into a finished product, eliminating the need for tooling and fixtures, opening the potential for crafting parts with intricate geometries that are challenging to attain through traditional manufacturing processes [8]. Consequently, the considerations for design in terms of manufacturing and assembly can be minimized, fostering design innovation. AM also promotes environmentally conscious product design [6]. In contrast to traditional manufacturing techniques that impose restrictions on design, the flexibility of AM empowers manufacturers to refine design for efficient production, inherently reducing waste [9]. Additionally, AM's capacity to fabricate intricate geometries allows for the consolidation of multiple separate parts into a single object [10]. Furthermore, the topologically optimized designs achievable through AM have the potential to enhance a product's functionality, consequently diminishing the energy, fuel, or natural resources required for operation [11]. To sum up, AM offers personalized components, diminished consumption of raw materials and energy, on-demand manufacturing, and a resilient supply chain network [12].

The generation of imperfections within AM components is a significant concern for critical operational uses [13]. If these imperfections are not eliminated, they can adversely affect the performance of AM components during their operational lifespan [14]. Consequently, comprehending the

✉ Muhammad Arif Mahmood
  mmahmood@mst.edu

1 Intelligent Systems Center, Missouri University of Science and Technology, Rolla, MO 65409, USA

2 Department of Mechanical and Aerospace Engineering, Missouri University of Science and Technology, Rolla, MO 65409, USA

mechanisms underlying the creation of defects in fusion-based processes becomes crucial in determining the appropriate process parameters tailored to the specific alloy system and the chosen processing method [15, 16]. Laser-based metal AM methods are primarily divided into two (a) laser powder bed fusion (LPBF) and (b) laser-directed energy deposition (LDED) [17, 18]. In LPBF, a thin layer of powder is uniformly spread over a building platform [19–21]. A focused laser energy source then selectively melts the powder onto a metal substrate, resulting in intricately shaped components with high geometric intricacy [22–24]. On the other hand, LDED employs controlled powder flow propelled by an inert gas through a set of nozzles, combined with a focused laser beam to construct relatively complete structures [25–27]. The processing conditions for AM can markedly differ not only between LPBF and LDED but also among different AM processing chambers [28–30]. The rapid cycles of heating, cooling, and solidification inherent in the fabrication of AM metal components lead to intricate microstructures and properties that can substantially diverge from those typically found in conventional wrought or cast components [31]. The intricate transitional conditions intrinsic to metal AM processing exert an influence on the resultant metallurgical integrity, microstructures, residual stresses, and distortions within the components [32]. The occurrence of instabilities during processing frequently contributes to the emergence of internal defects, diminishing the mechanical characteristics of the component and substantially compromise its overall performance [33]. Table 1 has been compiled for a comprehensive overview of defects and their diverse sources in laser-based metal AM process.

The most recent developments in machine learning (ML) and artificial intelligence (AI) can have a significant positive impact on AM [45]. Since every step of the AM process is completed digitally, data organization and collection are made easier [46–48]. However, AM is a highly automated process when it comes to design, process setup, and printing [49–51]. Numerous system data are generated as a result, which are challenging for humans to visualize and understand [52]. It becomes more difficult due to the enclosed setup, which makes it difficult to observe and keep track of the process [53–55]. Cracks, delamination, distortion, rough surfaces, lack of fusion, porosity, foreign inclusions, keyholes, and balling are just a few of the processing-related flaws that still plague the AM process today [56–58]. These flaws are typically caused by the layer-by-layer material deposition process. Some could cause the entire build to fail if they spread from one layer to the next. Researchers have worked very hard to keep track of printing defects before, during, and after. In this regard, ML offers a novel approach for overcoming the difficulties, as listed in Table 2. The ML is essential to improving defect identification in metal AM processes, according to

Table 1 Various defects in laser-based metal additive manufacturing processes

Defect type	Illustration	Defect source	Reference
Lack of fusion (LOF)	LOF defects are irregular, elongated shapes ranging in size from 50 μm to several millimeters.	Energy source and process parameters	[34, 35]
Keyhole (KEH)	In high-energy-density AM processes, KEH porosity is observed. KEHs can become unstable and repeatedly form and collapse, leaving voids inside the deposit composed of entrapped vapor.	Rapid melting of material due to operating conditions	[36, 37]
Gas porosity	When using LPBF, these defects are typically on the order of 5 to 20 μm, whereas in parts produced with LDED are typically larger in size (> 50 m).	Elevated solidification rates as well as gas content	[38, 39]
Solidification cracking (SC)	SC is a complex phenomenon that occurs near the end of solidification in the fusion zone. It is caused by a temperature gradient and the interaction of metallurgical and mechanical factors.	Phase transformation	[40]
Solid-state crack (SSC)	SSC is caused by the continuous heating and cooling of various metallic metals during the printing process.	Strong precipitation reactions	[41]
Impurities	During printing, impurities are likely to form oxides with alloying elements and contaminate material feedstocks.	Feedstock, and printing chamber conditions	[42]
Surface-connected pores (SCP)	SCPs are caused by earlier vapors that resurfaced as bubbles during material transport but solidified before closing the pore shape.	Design features	[43, 44]

all the studies [45, 59]. ML models can accurately classify defects in the printed parts by extracting meaningful features and patterns from the data collected during these processes [52, 60]. By identifying anomalies and deviations from regular patterns, these models make real-time monitoring, predictive maintenance, and process optimization possible [61, 62]. Additionally, ML is essential for developing practical solutions that boost metal AM product quality and dependability while streamlining quality control with automated and data-driven defect detection techniques [63].

Mostly, AM techniques include iterative testing to optimize the process, with the goal of producing defectless components while conserving resources. Due to the resource-intensive nature, however, AM has found limited uses in specialized fields. On the other hand, the development of AM process maps will increase the acceptance of AM in industrial applications. The fundamental goal of this research is to acquire a systematic approach that can be easily applied for process optimization. In particular, the LPBF technique for metal AM necessitates a consistent framework to determine process maps for specific materials or alloys. These process maps delineate zones with no macroscopic component defects. For this purpose, a novel framework that combines an experimentally validated finite element method (FEM) model with a backpropagation-based artificial neural network (BPANN) model has been presented. To fine tune the weights, BPANN uses the error rate of a forward propagation, with the goal of reducing error in comparison to other artificial neural network techniques [79]. The laser scan speed, laser power, powder bed thickness, pre-heating temperature of the powder bed, and temperature-dependent material parameters were all changed to develop a set of 81 simulations. The resulting dataset was used to train and test the BPANN. Following that, process maps were generated using the trained and tested BPANN model by varying the process parameters. Here, a process map commonly uses melt pool dimensions to determine inadequacies such as lack of fusion, balling, and keyhole flaws. After removing the indicated areas, any remaining zone was determined as a region where defect-free components can be obtained.

2 Proposed methodology

The method used to develop process maps is shown in Fig. 1. The groundwork was developed using a FEM model that included thermally dependent material parameters, laser power and scan speed, powder bed thickness, and pre-heating temperature of the powder bed. Experimental investigations were used to validate the proposed FEM model. The modification of the process parameters and data generation was then conducted by the experimentally validated simulation model. The data gathered from the validated simulation model was used to build, train, and assess backpropagation-based artificial neural network (ANN) model. Notably, the

Table 2 Various machine learning algorithms for defects identification in metal additive manufacturing

AM process	Materials	ML technique	Output	Reference
LPBF	Stainless steel 304	Deep belief network, multi-layer perceptron, and support vector machine	Melt pool regimes	[64]
LPBF	Stainless steel	Convolutional neural networks	Print qualities	[65]
LPBF	Stainless steel 316L	Support vector machine and convolutional neural networks	Defects in the molten tracks	[66]
LPBF	Zinc	Unsupervised ML	Melting conditions	[67]
LPBF	Inconel 718	Support vector machine	Keyhole and balling	[68]
LPBF	Stainless steel	Support vector machine	Defects' location	[69]
LPBF	Stainless steel 304	Deep belief network, convolutional neural networks, and multi-layer perceptron	Melt pool regimes	[70]
LPBF	Stainless steel 304	Deep belief network	Melt pool condition based on laser power	[71]
LPBF	Inconel 718	Gaussian mixture model	Detect faulty bars	[72, 73]
LPBF	Stainless steel 316L	K-means clustering	Overheating defects	[74]
LPBF	-	Random forest and support vector machine	Surface irregularities after print	[75]
LPBF	Inconel 718	Convolutional neural networks and support vector machine	Defects due to process conditions	[76]
LDED	Titanium alloy Ti6Al4V	Self-organizing map	Pores defects	[77]
LDED	Titanium alloy Ti6Al4V	Self-organizing map	Defect location	[78]

Fig. 1 Proposed methodology for current research
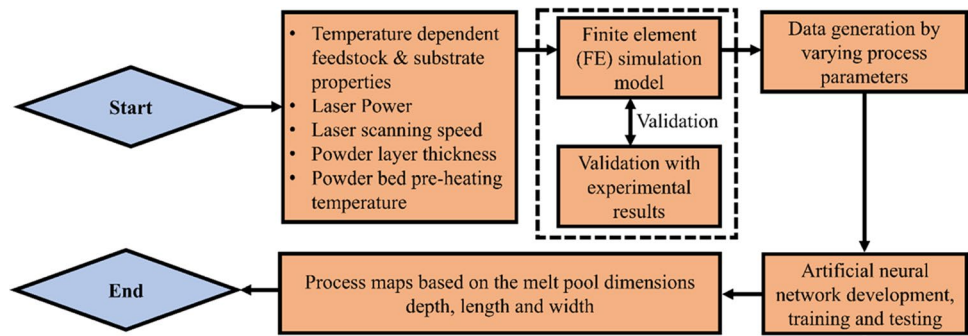
laser power and scan speed, powder bed thickness, and pre-heating temperature of the powder bed served as the ANN model's inputs, and the outputs were the melt pool's dimensional ratios. In compliance with the guidelines outlined in the following section, processing maps were developed using the trained and tested ANN model.

2.1 Modelling and simulation

Several assumptions were applied when establishing the heat distribution model for Inconel 718 (IN-718) process maps. To begin, a Gaussian-shaped moving heat source was used. The powder particles within the powder bed were spherical, allowing for the development of a highly dense powder bed. The dilution rate between the substrate and the printed layer was ignored throughout the printing process [80]. Increasing the dilution rate causes the substrate to have a higher impact on the composition dilution of the deposited layer, resulting in poor performance [80]. Furthermore, the printing process frequently introduces cracks and other defects. The ideal dilution between the deposited layer and the substrate during the printing process is between 2 and 10%, and can be ignored for modeling purposes [80]. During modeling, temperature-dependent thermo-physical parameters were incorporated in the simulations, ensuring precise and accurate simulation results. The transient heat equation in 3D can be written as [81, 82]:

$$\rho C_p \frac{\partial T}{\partial t} = \nabla(k\nabla T) + Q \tag{1}$$

In Eq. 1, T, C_p, ρ, and k are the thermal distribution, specific heat, density, and thermal conductivity. The temperature-dependent characteristics can be introduced as [81, 82]:

$$\frac{\partial T}{\partial t} = \frac{\partial T}{\partial x}\frac{\partial x}{\partial t} + \frac{\partial T}{\partial y}\frac{\partial y}{\partial t} + \frac{\partial T}{\partial z}\frac{\partial x}{\partial t} = \nabla T\vec{v} \tag{2}$$

Here, x, y, and z are the universal coordinates. Besides, the laser beam speed is expressed as $\vec{v}$. During printing process, heat losses have been considered as [81–83]:

$$Q = q_{rad} + q_{conv} + q_{laser\ beam} \tag{3}$$

$$q_{rad} = \varepsilon \sigma_B \left(T_{amb}^4 - T^4\right) \tag{4}$$

$$q_{cov} = h\left(T_{amb} - T\right) \tag{5}$$

$$q_{laser\ beam} = \frac{2AP}{\pi\sigma^2} e^{-\frac{2r^2}{\sigma^2}} \tag{6}$$

It worthy to mention here that Eqs. 4 and 5 are from ref. [83], Eq. 6 has been adopted from ref. [81] while Eq. 3 has been cited from ref. [82]. Here, σ_B, T_{amb}, ε, P, A, σ, h, and r are the Stefan-Boltzmann constant, room temperature,

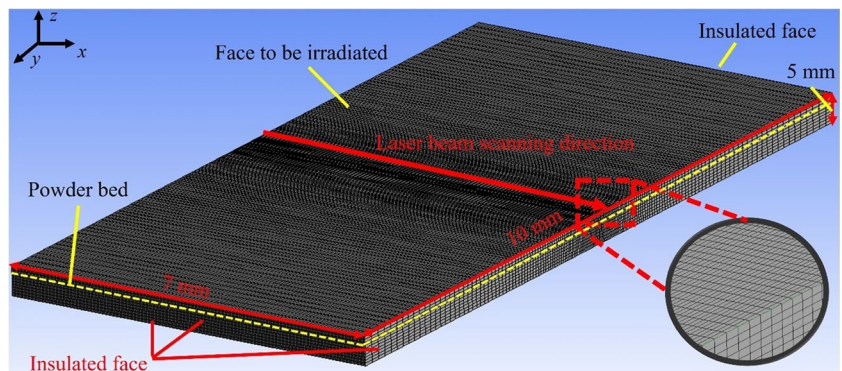**Fig. 2** Simulation model for process maps

Table 3 Inconel-718 properties [84, 85]

Temperature (°C)	Specific heat (J/kg)	Powder bed conductivity (W/m/°C)	Emissivity of powder bed
0	427	0.0966	-
20	427	0.0966	-
100	441	0.0981	-
300	481	0.100	-
500	521	0.102	-
538	-	-	0.46
649	-	-	0.59
700	601	0.1078	-
760	-	-	0.72
1350	691	0.1190	-

emissivity, laser power, laser beam absorptivity, beam radius, convection coefficient, and radial distance between the beam and point of material heat [81, 82]. For 7-mm layer deposition on a 10 mm × 7 mm × 5 mm substrate, ANSYS simulation software was used. The FE simulation domain by ANSYS software is compiled in Fig. 2. During solution, a mesh size of 0.0192 mm was applied based on the aspect ratio (= 0.9) and skewness (= 0.08), defining a good quality mesh. Here, aspect ratio defines the compression or tension in an element while skewness identifies the distortion or misalignment on an element's internal angle, having ideal values equal to 1 and 0, respectively. Temperature-dependent IN-718 properties were used during stimulation, as provided in Table 3. All the simulations were carried out on intel(R) Core (TM) i7-7700 CPU at 3.60 GHz, and 16 GB RAM. With the mentioned conditions, the results for one simulation were obtained in 1.5 h. To validate the FEM simulation model, the laser power was kept equivalent to 180 W; laser scanning speed equal to 400 mm/s, 600 mm/s, and 800 mm/s; and powder layer thickness equal to 40 µm. Following the model validation, a design of experiment (DoE) was developed and carried out using validated FEM model. The

DoE included changing the laser power from 50 to 250 W with an interval of 50 W; laser scanning speed from 500 to 2500 mm/s with an interval of 500 mm/s; powder layer thickness was kept equal to 30, 50, and 70 µm; and powder bed pre-heating was equivalent to 60, 90, and 120 °C. For thermal distribution, all the calculations have been carried out in degree Celsius (°C).

The other parameters used in the simulation are compiled in Table 4.

2.2 Experimental validation

A comparison between the current simulation model and experiment described in ref. [90] was conducted to determine the reliability of the proposed simulation model. The authors used a Nd:YAG laser with a 54-µm laser spot on a Tongtai AM250, Taiwan, system for LPBF investigations. The specifications of Tongtai AM250 are provided in Table 5.

A laser power = 180 W and laser scanning speed = 400, 600, and 800 mm/s were used to prepare single layer specimens. For each sample, the powder layer thickness was 40 µm. The dimensions of the melt pool were measured using a Nikon AF-S high-speed CMOS camera. The camera was positioned 40° away from the build chamber at 35 cm. The camera was carefully calibrated before the experimentation. Additionally, an optical filter with a spectral range of 788–828 nm was installed on the camera to eliminate the high-frequency signal and enhance the image quality. More information can be read in ref. [90].

2.3 Process sensitivity analyses using validated FEM model

Table 6 compiles the design of experiment carried out using experimentally validated FEM model. These simulations included changing the laser power from 50 to 250

Table 4 Operating conditions used in simulation model

Operating condition	Index	References
Room temperature	28 °C	-
Gas conductivity	0.016 W/m/°C	[86]
Coefficient of convection	15 W/m²/°C	[87]
Substrate density	8146 kg/m³	[84]
Laser beam absorption coefficient	0.45	[88]
Fusion latent heat	2.27×10^5 J/kg	[89]
Liquefaction temperature	1337 °C	[89]
Solidification temperature	1255 °C	[89]
Powder particles mean diameter	44 µm	-

Table 5 Specifications of Tongtai AM250 [91]

Specification	Illustration
Building chamber	$250 \times 250 \times 250$ mm³
Laser type	Fiber laser with 300 W
Scanning speed	10 m/s max.
Beam diameter	50–100 µm
Layer thickness	20–50 µm
Gas consumption during process	2 l/min
Dimensions	$1840 \times 1450 \times 2200$ mm³
Weight	1650 kg
Control software	Tongtai AMCS
Data preparation software	Magics, Tongtai build processor

Table 6 Design of experiment for simulation analysis

Laser power (W)	Laser scanning speed (mm/s)	Powder layer thickness (µm)	Powder bed pre-heating temperature (°C)
50	2500	30	60
200	2000	30	60
50	2000	30	60
200	1500	30	60
50	1500	30	60
100	1000	30	60
100	500	30	60
250	2000	30	60
100	2000	30	60
200	2500	30	60
150	1500	30	60
200	1000	30	60
250	500	30	60
50	500	30	60
150	2000	30	60
250	1000	30	60
150	500	30	60
100	1500	30	60
250	2500	30	60
150	2500	30	60
100	2500	30	60
250	1500	30	60
150	1000	30	60
50	1000	30	60
200	500	30	60
250	2000	50	90
100	2000	50	90
200	1000	50	90
100	500	50	90
250	2500	50	90
50	500	50	90
100	2500	50	90
200	2500	50	90
50	1500	50	90
250	1000	50	90
150	500	50	90
250	1500	50	90
200	1500	50	90
50	2000	50	90
100	1000	50	90
50	1000	50	90
250	500	50	90
100	1500	50	90
150	2500	50	90
50	2500	50	90
150	1500	50	90
150	1000	50	90
200	500	50	90

Table 6 (continued)

Laser power (W)	Laser scanning speed (mm/s)	Powder layer thickness (µm)	Powder bed pre-heating temperature (°C)
200	2000	50	90
150	2000	50	90
50	1000	70	120
200	500	70	120
250	2500	70	120
200	2000	70	120
200	2500	70	120
150	1500	70	120
150	2000	70	120
150	1000	70	120
250	500	70	120
100	500	70	120
150	2500	70	120
50	2500	70	120
250	2000	70	120
250	1000	70	120
100	1500	70	120
50	500	70	120
200	1500	70	120
50	1500	70	120
250	1500	70	120
200	1000	70	120
100	1000	70	120
150	500	70	120
100	2500	70	120
100	2000	70	120
50	2000	70	120

W with an interval of 50 W; laser scanning speed from 500 to 2500 mm/s with an interval of 500 mm/s; powder layer thickness was kept equal to 30, 50, and 70 µm; and powder bed pre-heating was equivalent to 60, 90, and 120 °C. The artificial neural network model was trained and tested using the outcome of these simulations.

2.4 Backpropagation-based artificial neural network development

The artificial neural network (ANN) is made up of interconnected processing elements with configurable connectivity weights that are fine-tuned during the learning phase. Each input in the ANN framework is assigned a weight that represents the strength of the connection between units. Individual nodes combine these weighted inputs and use an activation function to translate them into outputs. A backpropagation training approach is used to construct the architecture and optimize the network weights, which has proven superior capability in computing various Boolean functions

when compared to networks with a single layer of calculating units. The backpropagation algorithm is divided into two phases: (a) forward and (b) backward propagations. The key operational factors in our ANN model were laser power and scan speed, powder bed thickness, and pre-heating temperature of the powder bed. These parameters were fed into the ANN model as inputs. Among the several architectures tested, the 4-15-3 ANN model performed exceptionally well [92, 93]. The number of nodes in the input, hidden, and output layers is represented by the notation 4-15-3. The employed learning rate coefficient was set to 0.01.

2.5 Processing window criteria

Lack of fusion is utilized to recognize inter-layer joining for a given material, and defined by using melt pool dimensions [94]. To successfully bond a deposited layer to a prior layer, melt pool depth (D) should surpass powder bed thickness (t) and adequately remelt the previously deposited layer. The smallest value of lack of fusion for confirming link between two subsequent deposition is equal to 1, implying that D should equal t, which is, however, insufficient for proper bonding. One recent study [95] found 99.9% dense AM portions of Ti6Al4V, showing proper inter-layer bonding. The lack-of-fusion value was calculated to be 1.15. As a result, a penetration of 15% of t into the prior layer indicates strong inter-layer joining. Hence, for lack of fusion to appear in IN-718, the criterion was referenced as $D/t \leq$ 1.15. In keyhole, the energy density is adequate to foster metal evaporation causing cavity formation [96]. The plasma formation due to metal evaporation results in an increased laser absorption. According to Roehling et al. [97], keyhole usually occurs at an aspect ratio of $W/D < 1.5$, where W indicates width of the melt pool. This value, however, is insignificant to display within the processing window [12,

98]. As a result, the keyhole requirement for IN-718 was chosen as $W/D = 2.0$. Balling is a defect caused by the inadequate wetting between the solidified deposited layer and the substrate, leading to uneven tracks [82, 99]. Balling can be linked with the melt pool dimensions calculated as L/W > 2.1. This threshold value can be linked to the Plateau-Rayleigh uncertainty in molten material. Figure 3 presents a schematic approach to select hatch distance after selecting operating conditions based on melt pool dimensions.

3 Results and discussion

Figures 4a and b depict the sequential evolution of the melt pool during LPBF of IN-718, illustrating the powder layer's early, middle, and final stages. The dynamic changes in the thermal distribution profiles along the laser scanning path (from left to right) can also be observed in the Fig. 4. The LPBF was carried out via laser with a power of 180 W and scan speed of 400 mm/s. During simulation, the powder bed thickness was 40 µm. It is important to mention here that the properties used in the FEM model are temperature dependent. Hence, phase change can be identified in Fig. 4 using different codes, including red color code for melt pool, green color for mushy zone, and light blue color for the solidified region. The isotherm curves show the temperature at which IN-718 melts. The material reaches its melting point at the highest temperature indicated by the isotherm, creating an asymmetrical melt pool marked by a series of ellipses. The laser beam's energy is transported through the material, resulting in an unequal distribution of isotherms, with more significant generation noted towards the front compared to the rearward region. When the laser is positioned at the start, the temperature within the powder layer exceeds the melting

Fig. 3 Schematic approach to print near-dense components after selecting operating conditions based on melt-pool dimensions
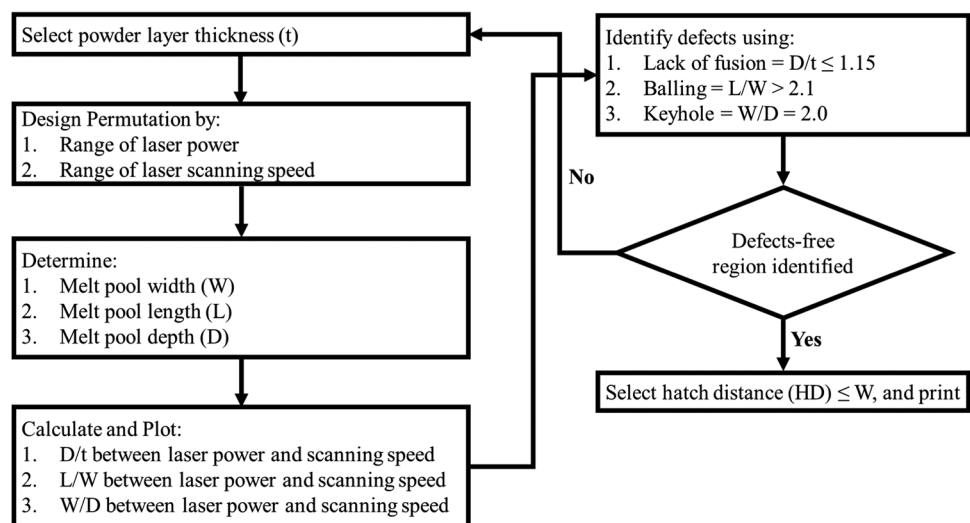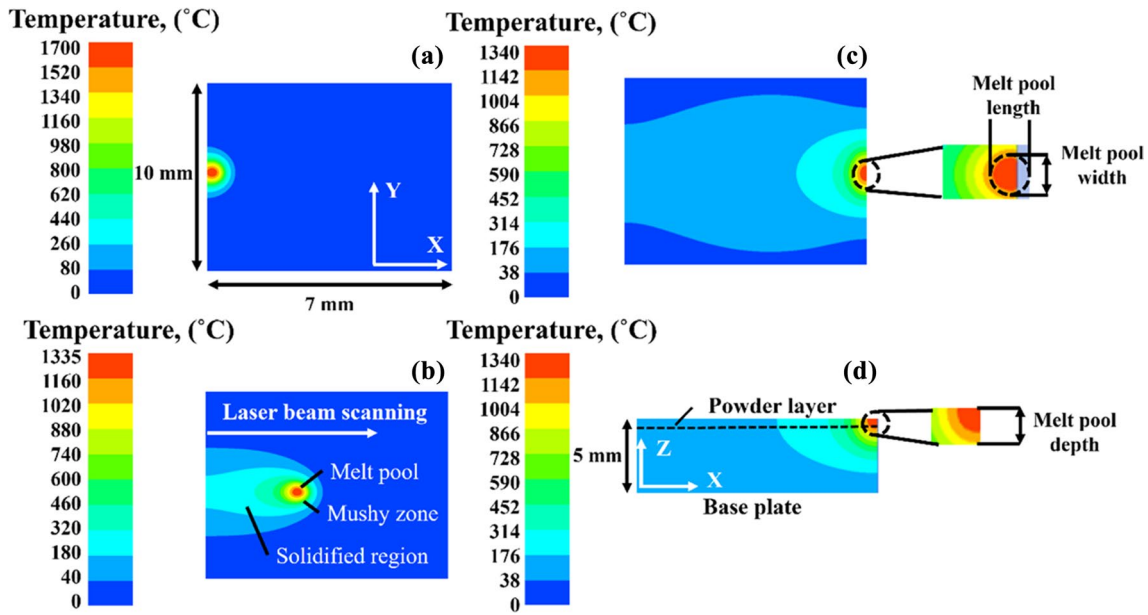
Fig. 4 Single-layer LPBF simulation of Inconel-718 at **a** start, **b** intermediate, **c** end of the scan, and **d** melt pool depth at the end of the laser scan

temperature of IN-718, reaching up to 1700 °C in Fig. 4a. It is due to the material's lower heat conductivity within the laser-material regime, which causes localized melting. However, as the beam advances, the peak thermal distribution drops to 1335 °C at the center and 1340 °C at the end of the powder bed. Heat transfer from the powder bed to the base plate causes this decrease, which stabilizes the temperature distribution. Figure 4d depicts the temperature evolution across the powder bed.

The developed simulation model was validated with the experimental and simulation analyses from ref. [90]. The authors in ref. [90] used in situ CMOS camera to measure melt pool width and length. Figures 5a and b show a comparison for melt pool's length and width. For samples 1, 2 and 3, laser power was kept equal to 180 W while laser scanning speed was selected as 400 mm/s, 600 mm/s, and 800 mm/s, respectively. From the results, it can be identified that the FEM model presented a reliable solution for melt pool length and width compared to the experimental analyses. It is worthy to mention here that the accuracy of FEM simulation model depends on the modelling details, mesh quality, boundary and initial conditions, material properties,
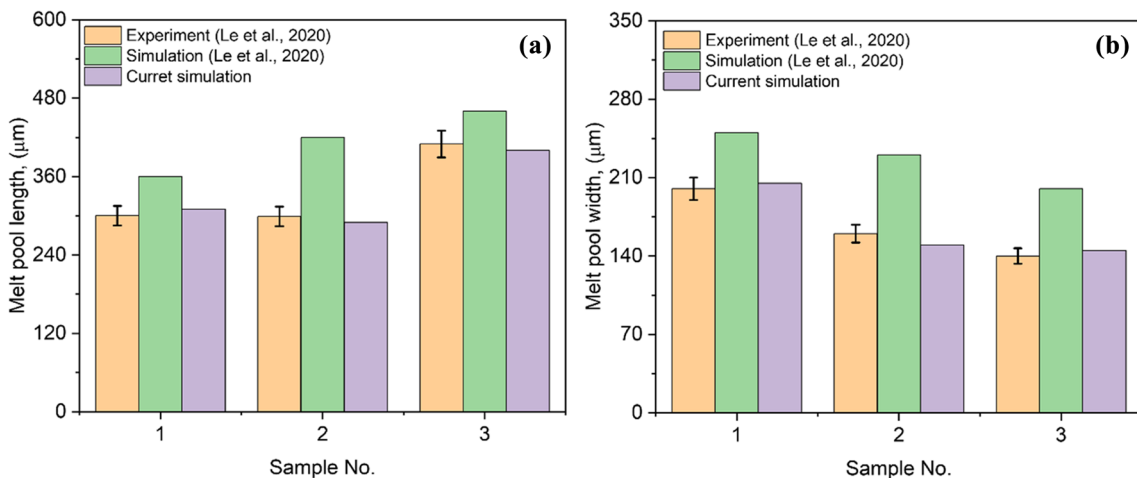

Fig. 5 Inconel-718 laser powder bed fusion current FEM model validation with published experimental [90] and simulation [90] data for melt pool **a** length and **b** width

and software module. As explained above, the authors have used temperature-dependent properties along with the well-structured and appropriately refined mesh size in current simulation. To replicate the LPBF printing process in simulation environment, the non-linear transient heat transfer analysis with well-defined initial and boundary conditions has been applied in the ANSYS software. Hence, it can be observed that the accuracy of current simulation model is close to the experimental results compared to those provided in ref. [90] utilizing linear simulation framework.

After FEM model had been experimentally validated, the simulations were conducted using the design of experiment presented in Table 6. Figure 6 shows a correlation chart that was generated using the collected data. The relationship between inputs (laser power, powder layer thickness, powder bed pre-heating temperatures) and outputs (average melt pool depth, length and width) has been produced on a correlation chart. A perfect positive correlation between the two items is shown by green, whereas a perfect negative correlation is shown by red in the correlation chart. Due to an increased energy transfer from the laser beam to the material with a surge in the laser power, a positive correlation among laser power, average melt pool depth, length, and width has been identified. On the other hand, due to the shortened laser-material contact period caused by an increased laser scanning speed, average melt pool depth, length, and width were negatively correlated with laser scanning speed. Additionally, a negative association between layer thickness and average melt pool depth has been found; however, no correlation between layer thickness and average melt pool length or width has been found. Additionally, it has been shown that the powder bed pre-heating temperature and average melt pool depth have a significant positive correlation that is on the verge of being strongly inversely correlated with the average width of the melt pool. Based on the results, it is evident that an excessive powder bed pre-heating temperature causes the melt pool to grow deeper and narrower, which encourages defects during printing. To reduce thermal stresses in the powder bed while preventing defects during LPBF, it is crucial to establish the ideal temperature for pre-heating the powder bed.

A correlation chart was developed in Fig. 7 using the data from the FEM simulations to examine the correlations between the input parameters of laser power and scan speed, powder bed thickness, and pre-heating temperature of the powder bed, and the output parameters having ratios of average melt pool depth to powder layer thickness (D/t), average melt pool length to melt pool width (L/W), and average melt pool width to melt pool depth (W/D). As these ratios are critical for determining printability, it is important to note that the selection and computation of D/t, L/W, and W/D values were exclusively based on the melt pool's dimensions. A color-coding scheme was used in the correlation chart, with blue denoting a high positive correlation, red denoting a strong negative correlation, and white denoting no significant connection between the two quantities. After investigation, it was shown that laser scanning speed showed only weak associations with L/W and W/D and a strong negative connection with D/t. In the case of D/t, L/W, and W/D, respectively, laser power showed positive, strongly positive, and no relationships. The analysis also exhibited the correlations among the powder layer thickness, D/t, L/W, and W/D. It showed a weakly negative association with D/t as well as W/D while a weak correlation with L/W ratio. The powder bed pre-heating temperature presented a very weak connection with D/t, L/W, and W/D ratios.

The design of experiment provided in Table 6 was used to run simulations via the experimentally validated model. For training and testing, the simulation data was fed into an artificial neural network (ANN) via backpropagation. The ANN model was developed using MATLAB software. Inputs to the ANN model were laser scanning speed, laser power, powder layer thickness, and powder bed pre-heating temperatures, while outputs included D/t, L/W, and W/D ratios, which provided useful insights on process maps. To

	Laser power (W)	Laser scan speed (mm/s)	Layer thickness (μm)	Powder bed pre-heating (°C)
Average melt pool depth (mm)	0.9	-0.51	-0.6	0.88
Avergae melt pool length (mm)	0.6	-0.16	-0.004	0.2
Avergae melt pool width (mm)	0.71	-0.22	-0.003	-0.61

Fig. 6 Correlation between process inputs and outputs

	Laser scanning speed (mm/s)	Laser power (W)	Powder layer thickness (μm)	Powder bed pre-heating (°C)
D/t	-0.49	0.4	-0.58	-0.02
L/W	0.087	0.9	0.25	0.029
W/D	0.03	0.029	-0.29	-0.052

Fig. 7 Correlation between process inputs ((laser power, layer thickness, and powder bed pre-heating temperature) and melt pool dimensional ratios (D/t, L/W, and W/D; D = average depth, L = average length, W = average width, and t = powder layer thickness)

Fig. 8 Artificial neural network training based on the simulation analysis **a** mean squared error and **b** gradient plot
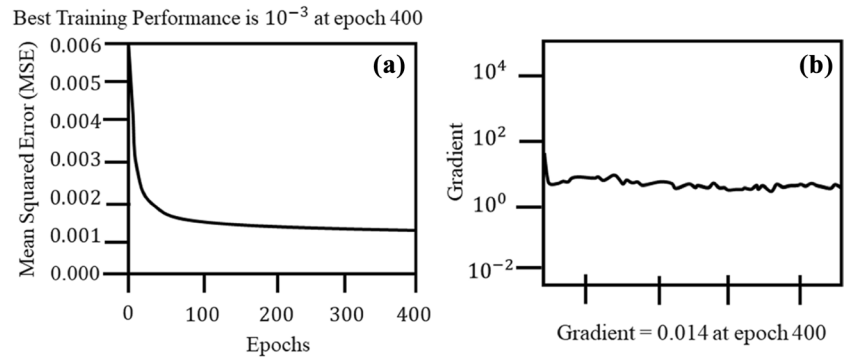
ensure robust model development, the complete dataset was divided into 70% (for training) and 30% (for testing). A total of 400 epochs were carefully chosen for the iterative training of the ANN model. Following that, the model achieved a low mean squared error (MSE) of 0.001 and a gradient of 0.014 at epoch 400, as shown in Fig. 8a and b, respectively. Following the completion of the training procedure, the trained

ANN model was applied to a parametric investigation by systematically altering the operating conditions.

After the training and testing of ANN, a parametric sensitivity analysis was conducted employing the ANN model to investigate the impact of varying operational parameters on the LPBF process. These parameters encompassed laser power and scan speed, powder bed thickness, and
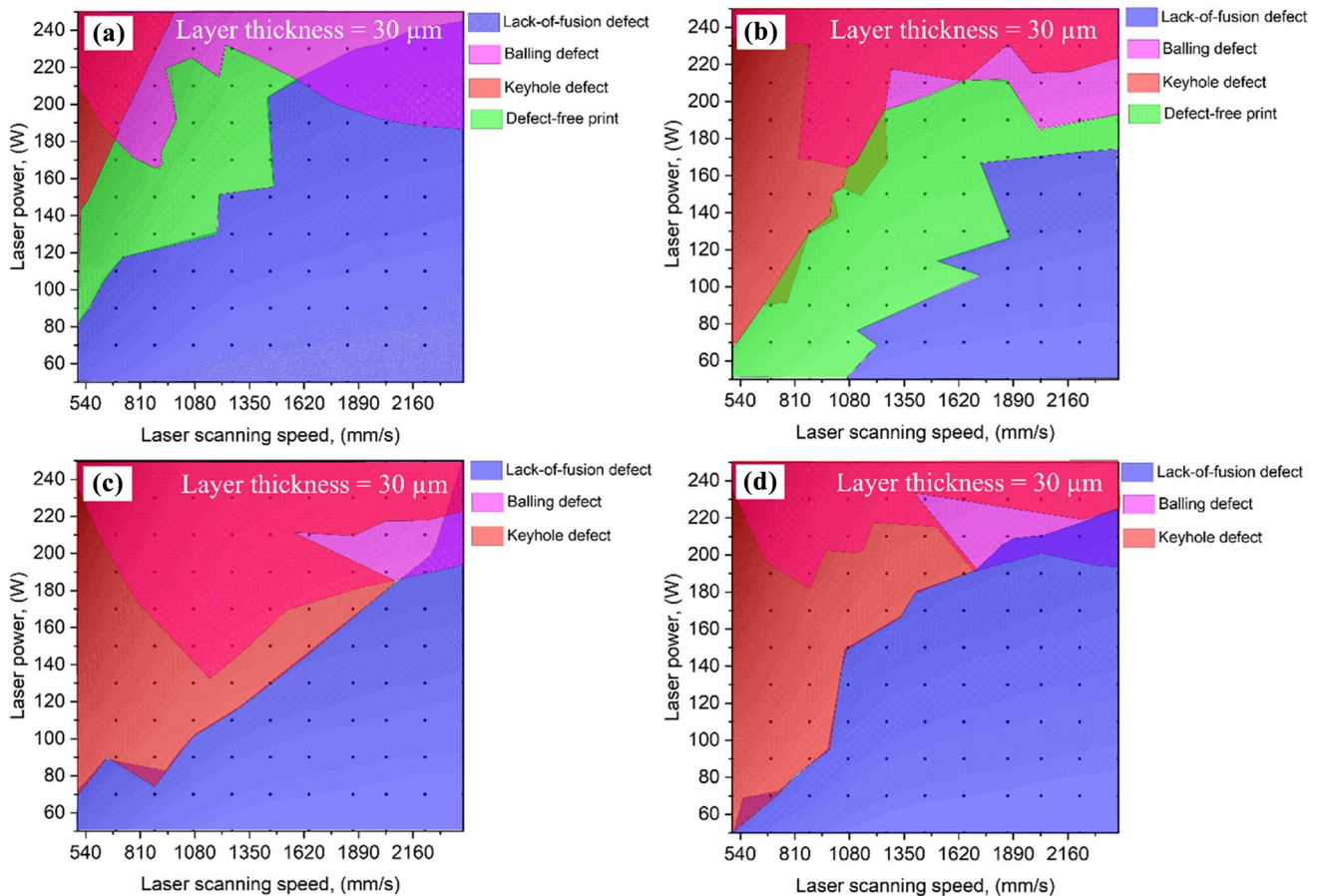
Fig. 9 Printability maps of Inconel-718 with layer thickness = 30 µm when powder bed pre-heating temperatures are **a** 120 °C, **b** 90 °C, **c** 60 °C, and **d** 30 °C

pre-heating temperature of the powder bed. Figures 9a–d exhibit the effect of powder bed pre-heating temperature on the processing region defined as the region obtained after excluding lack-of-fusion, balling, and keyhole defect areas, at temperatures of 120 °C, 90 °C, 60 °C, and 30 °C, respectively. In literature, researchers have developed processing regions using energy density for 7075 aluminum and TiC, tungsten, and tungsten-based alloys [100–102]. However, in this study, processing windows have been developed between laser power and scan speed. By developing a process map, using laser power and scan speed provides several benefits. These parameters streamline printing process setup and fine tuning, promoting improved process insight. The impact of process characteristics such as laser power and scan speed on the printing process can be observed individually, assisting in process optimization. This technique allows for adaptable processing conditions, simplifying experimental design and understanding of the LPBF system. While energy density has significant applications, focusing on laser power and scan speed increases process control, flexibility, and insight into the LPBF process. At a temperature of 120 °C for powder bed pre-heating, the predominant defect

observed is lack of fusion with the availability of printability region, which can be further categorized as either lack-of-fusion root or lack-of-fusion sidewall [103]. In the lack-of-fusion root defect, the deposited layer fails to adequately fuse with the base plate, while in the lack-of-fusion sidewall defect, the deposited layer in immediate proximity to the base plate fails to adhere properly [103]. The utilization of a powder bed pre-heating temperature can alleviate thermal stresses, minimize distortion in the printed components, and reduce thermal gradients generated during the printing process [104]. Nevertheless, excessively high powder bed pre-heating temperatures can give rise to excessive thermal gradients, causing the printed layer to immediately adhere to the base plate, resulting in lack-of-fusion sidewall defects [105]. As the powder bed pre-heating temperature decreases from 120 to 90 °C, the lack-of-fusion region notably diminishes in comparison to the region observed at 120 °C. However, the printability and keyhole-based defect regions increase significantly compared to 120 °C. As the temperature further decreases from 90 to 60 °C, it becomes evident that keyhole-based defects dominate over lack-of-fusion and balling defects. The predominance of keyhole-based defects can be
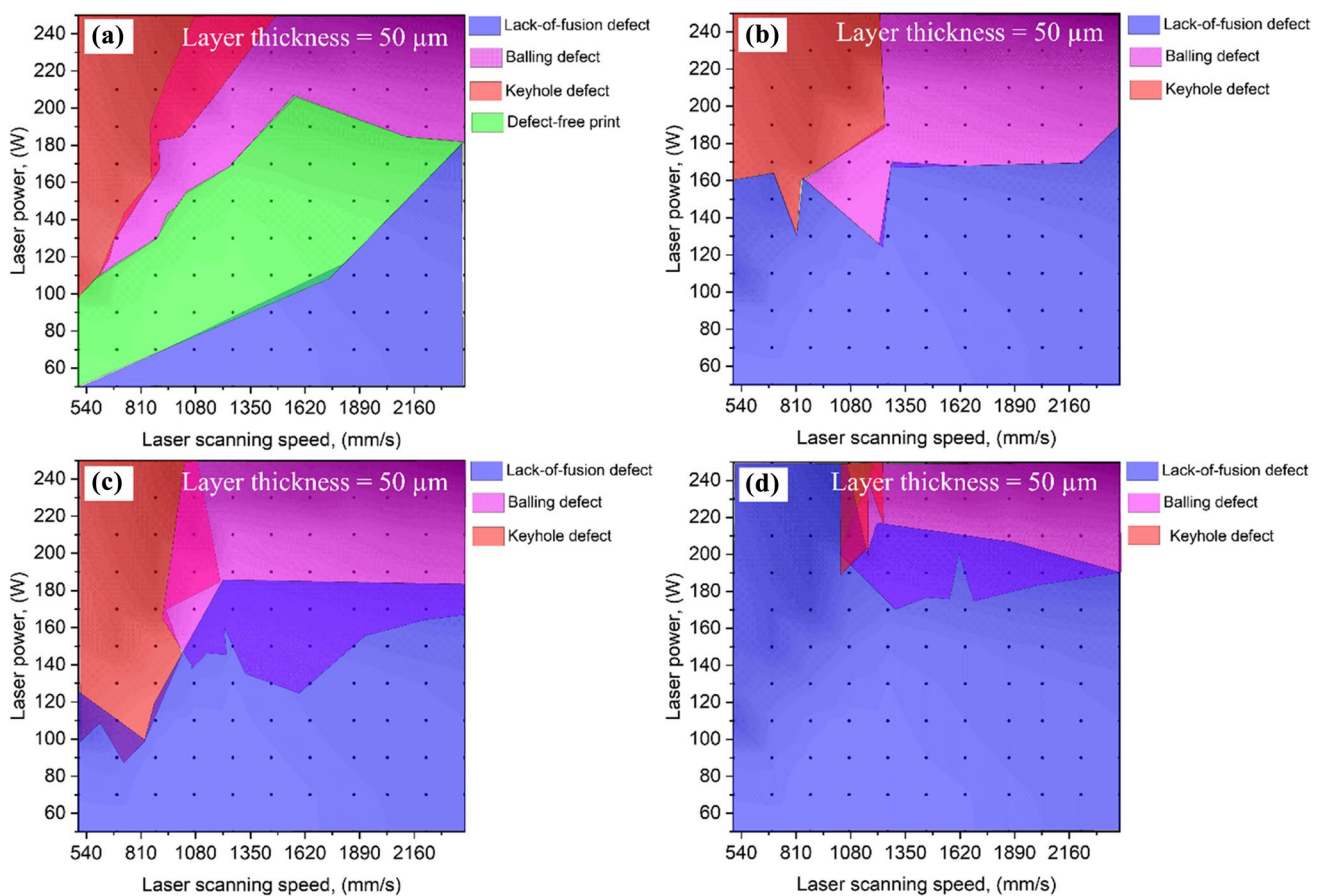

Fig. 10 Printability maps of Inconel-718 with layer thickness = 50 μm when powder bed pre-heating temperatures are **a** 120 °C, **b** 90 °C, **c** 60 °C, and **d** 30 °C

explained by the correlation between sub-atmospheric pressure and thermal gradients. A linear relationship was identified between sub-atmospheric pressure and thermal gradients, where a decline in sub-atmospheric pressure leads to a rise in the depth of the molten pool, transforming conduction melt flow from to depression mode [106]. A very low sub-atmospheric pressure stabilizes the keyhole during the laser printing process. Conversely, at a powder bed pre-heating temperature of 30 °C, no defect-free region was achieved, and lack-of-fusion defects prevailed over balling and keyhole defects. In this case, the lack-of-fusion root defect was identified due to insufficient powder bed pre-heating temperature as well as the operating conditions that did not permit thorough melting of the powder layer.

The printability maps produced by the trained ANN model for 50-µm powder layer thickness with different pre-heating temperatures of the powder bed (120 °C, 90 °C, 60 °C, and 30 °C) are shown in Fig. 10a, b. It can be observed that after increasing the powder layer thickness from 30 to 50 µm, powder bed pre-heating temperature = 120 °C provided printable region besides having lack-of-fusion, balling, and keyhole defects. When the powder bed pre-heating

temperature is lowered to 90 °C, the printability region vanishes, and lack-of-fusion defects become more common. This issue can be ascribed to the 90 °C temperature in combination with other operating conditions not being enough to completely melt the powder layer. Similar outcomes can be seen at 60 °C and 30 °C powder bed pre-heating temperatures, where lack-of-fusion defects predominate because of the insufficient energy density offered, preventing full melting of the powder layer.

The impact of different powder bed pre-heating temperatures, specifically 120 °C, 90 °C, 60 °C, and 30 °C, on the printability maps for a powder layer thickness of 70 µm has been illustrated in Fig. 11a–d utilizing the trained ANN model. At 120 °C, a higher proportion of defects related to keyhole formation and balling are observed compared to lack-of-fusion defects. This observation can be attributed to the direct relationship between powder bed pre-heating temperatures and the depth of the molten pool, which influences the flow of molten material, resulting in non-uniformity of the molten pool and promoting the occurrence of balling and keyhole-based defects. As the powder bed pre-heating temperature is decreased from 120 to 90, 60, and 30 °C, a
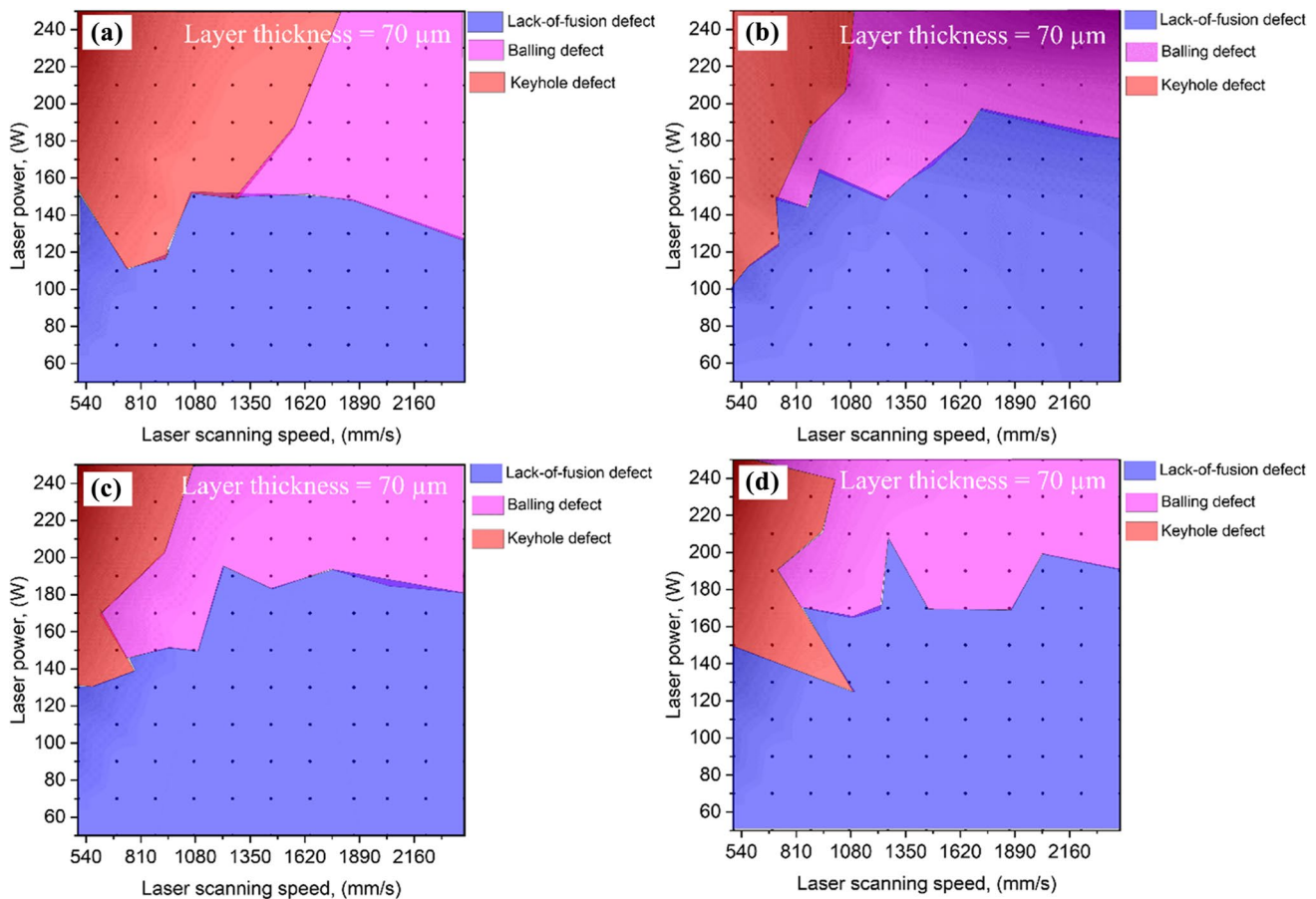

Fig. 11 Printability maps of Inconel-718 with layer thickness = 70 µm when powder bed pre-heating temperatures are **a** 120 °C, **b** 90 °C, **c** 60 °C, and **d** 30 °C

larger region is dominated by lack-of-fusion defects rather than balling and keyhole defects. This outcome arises due to the combination of a thicker powder layer and lower powder bed pre-heating temperature, which hinders the propagation of thermal intensity across the powder bed, consequently leading to the absence of defect-free regions. Lack of fusion usually occurs when the provided energy density is not adequate to melt the given powder layer. In Fig. 11d, the combination of process parameters such as laser power = 50–150 W, laser scanning speed = 540–1080 mm/s, and powder layer thickness = 70 μm, the provided energy is not enough to melt down the given material. However, while moving from laser power = 150 W to onwards, laser scanning speed = 540–1080 mm/s, and powder layer thickness = 70 μm, the operating conditions moved the LPBF printing process from conduction mode to keyhole mode.

Figures 12a–d depict the printability maps obtained for a powder layer thickness of 100 μm at various powder bed pre-heating temperatures, including 120 °C, 90 °C, 60 °C, and 30 °C, utilizing the trained ANN model. The analyses reveal the predominance of lack-of-fusion and balling defects under all operating conditions, with no region exhibiting successful prints. It is crucial to note that, in the case of a 100-μm powder layer thickness, the powder bed pre-heating temperatures fail to establish a molten pool with a stabilized and deep thermal gradient required for complete melting of the powder layer. Consequently, lack-of-fusion and balling defects arise. Keyhole-based defects are not observed under the given conditions since the molten pool does not attain sufficient depth to achieve complete melting throughout the powder layer. Therefore, selecting a 100-μm powder layer thickness is not logical for defect-free component printing.

LPBF experimental investigations were carried out to validate the outcomes provided by the ANN model, as provided in ref. [107]. The results are compiled in Fig. 13a–c. Figure 13a shows the processing map developed using ANN, Fig. 13b compiles the experimental results from ref. [107], and Fig. 13c exhibits the keyhole from Fig. 13b. According to the processing maps, the operating conditions highlighted as "1 and 2" have been identified as the conditions providing keyhole and lack-of-fusion defects, respectively. The output of the conditions 1 and 2 can be counter-verified from Fig. 13b
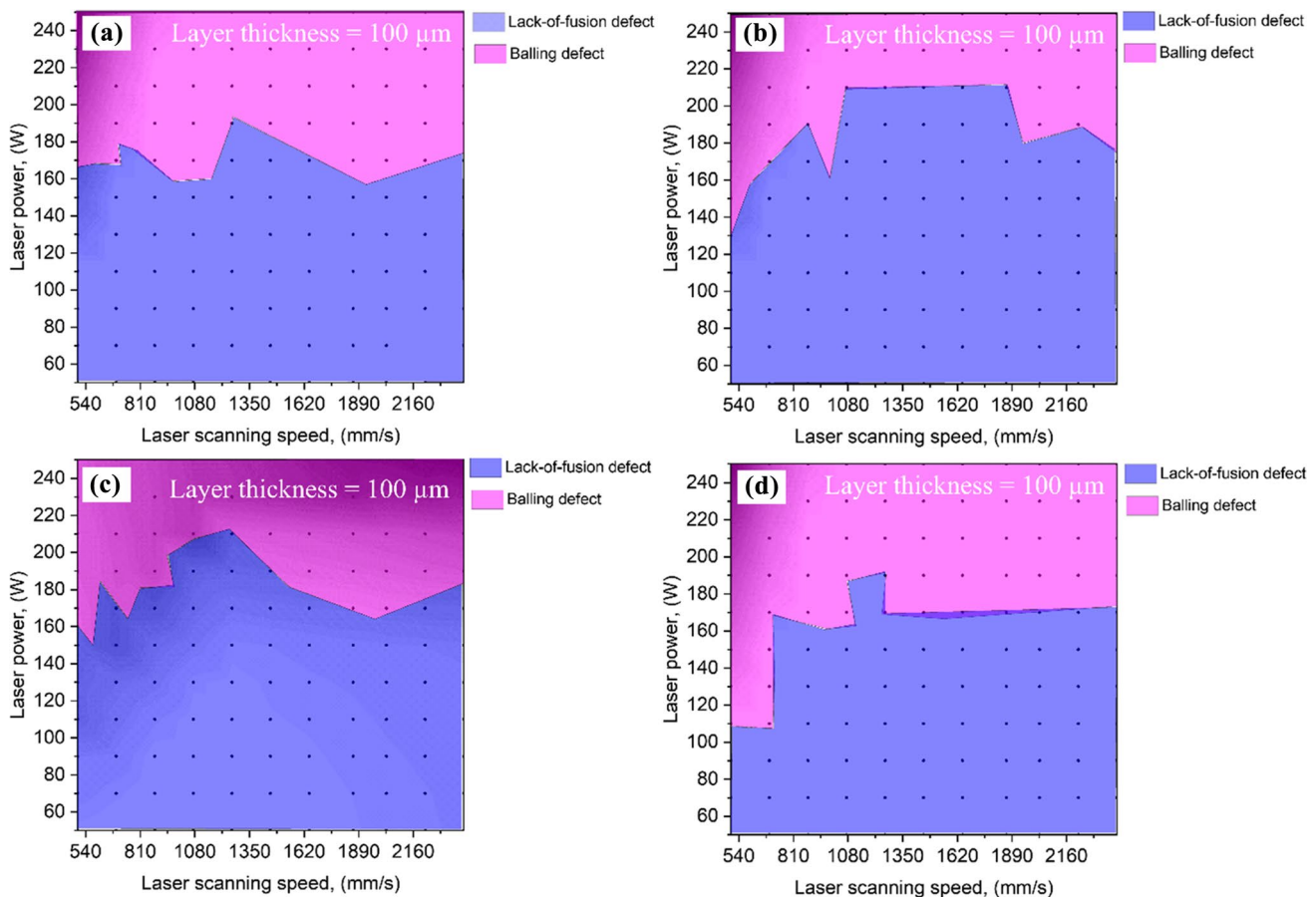

Fig. 12 Printability maps of Inconel-718 with layer thickness = 100 μm when powder bed pre-heating temperatures are **a** 120 °C, **b** 90 °C, **c** 60 °C, and **d** 30 °C
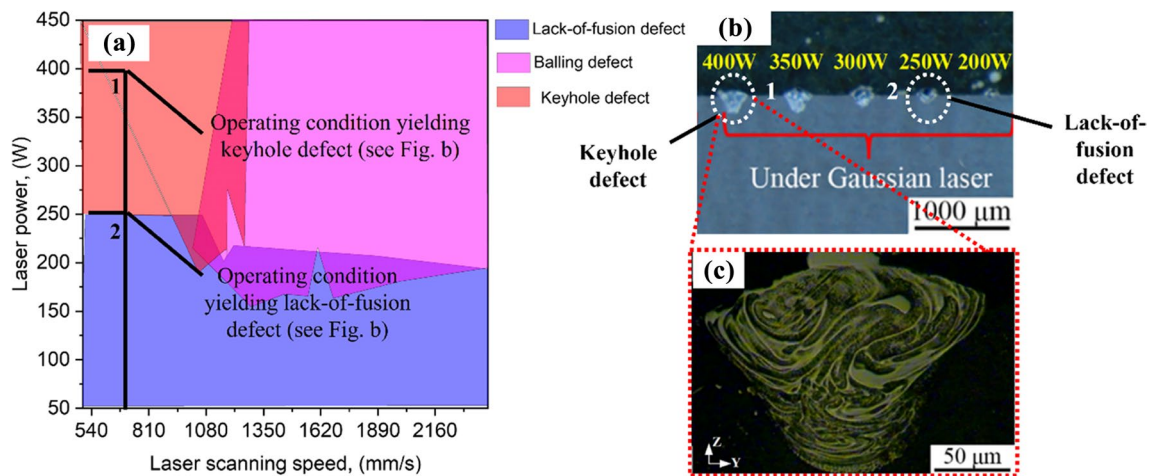
Fig. 13 Verification of **a** Inconel-718 processing maps using laser powder bed fusion, **b** experimental analyses with laser scanning speed = 600 mm/s and powder layer thickness = 50 μm [107], and **c** keyhole for laser power = 400 W, laser scanning speed = 600 mm/s, and powder layer thickness = 50 μm [107]; **b** and **c** with permission from publisher

as well. In Fig. 13a, distinct regions were defined using the given criteria. The lack-of-fusion defects have been highlighted using light purple hue. Meanwhile, keyhole defects are represented by the light red color code. Furthermore, the dominating defect, known as balling, caused by capillary instabilities inside the molten pool, has been highlighted using the color bright pink. The absence of a defect-free zone was identified under the stipulated operational parameters of room temperature at 30 °C and powder layer thickness of 50 μm. When the process maps obtained from the trained and tested ANN model are compared to experimental analyses, the ANN has showed exceptional reliability. One of the primary benefits of the trained ANN model is its capacity to efficiently monitor the impact of operational variables on outcomes, outperforming simulations, and experimental studies, resulting in significant time and cost savings.

4 Conclusions and outlook

In this study, the FEM simulation model was integrated with the backpropagation ANN machine learning model. Initially, the FEM model was validated experimentally and, later, used to develop a dataset for ANN training. This combination aided in the development of processing maps for Inconel-718 using LPBF while considering crucial parameters such as laser power, scan speed, powder layer thickness, and powder bed pre-heating temperature. Melt pool characteristics, including depth, length, and width, were used to designate zones prone to defects such as lack-of-fusion, balling, and keyhole.

- It has been identified that, in addition to operating conditions, the powder bed thickness and pre-heating temperatures played important roles in defect formation. Excessive pre-heating and thick powder layers were found to increase these undesired defects. As for laser power and laser scanning speed, their effects on the molten pool dimensions have been well established; higher laser power or reduced scanning speed leads to an enlarged molten pool. Moreover, elevated powder bed pre-heating temperatures were observed to increase the melt pool depth, transforming its mode from conduction to keyhole. Comprehensive processing maps were generated using the trained and validated ANN model, which revealed that regions with zero defects could be achieved under specific conditions: (a) a powder bed thickness of 30 μm at 120 and 90 °C pre-heating temperatures and (b) a powder bed thickness of 50 μm at a 120 °C pre-heating temperature. However, no healthy prints were achieved for powder layer thicknesses of 70 and 100 μm.

- LPBF processing maps provide vital insights by allowing for precise predictions of printed part quality and reliability. These maps essentially function as a set of recommendations for improving prints by fine-tuning operating conditions. A dense part is built utilizing the LPBF technique by selectively melting and fusing successive layers of powder. However, this technique frequently entails trial and error, which may risk the final part's strength, precision, and surface polish. To reduce such hazards, processing maps can be used to systematically optimize process parameters. In conjunction with processing maps, the suggested method helps the determination of optimal parameters for generating defect-free components. Using processing maps as a starting point, it is possible to successfully turn a single-layer design into a multi-layer structure by selecting appropriate parameters, such as hatch distance.

- The developed model and technique can be used to develop processing maps for other material systems as well, including Al [100] and refractory materials [100] in the case of the LPBF process. To achieve reliable results, it is extremely important to determine the thermo-physical properties of the given material system. Currently, the developed model cannot predict hot cracking issues in the LPBF process. However, the FEM model can be extended to calculate the distance between liquidus and solidus temperatures (DLST) [108]. The cracking susceptibility will be lower if the DLST value is small. For process automation, the ML model can be developed by providing operating conditions as an input while the outcomes, including DLST, as an output. This approach will result in the hot cracking identification framework [109–111]. Another domain that can be explored in the near future is to link the subtractive manufacturing with AM to identify the effect of machining on features' shape and size in the AM components [112].

Declarations

References

1. Sing SL, Yeong WY (2020) Laser powder bed fusion for metal additive manufacturing: perspectives on recent developments. Virtual Phys Prototyp 15:359–370. https://doi.org/10.1080/17452759.2020.1779999
2. Jinoop AN, Subbu SK, Kumar RA (2018) Mechanical and microstructural characterisation on direct metal laser sintered Inconel 718. Int J Addit Subtractive Mater Manuf 2:1. https://doi.org/10.1504/IJASMM.2018.093250
3. Shi J, Zhao B, He T, Tu L, Lu X, Xu H (2023) Tribology and dynamic characteristics of textured journal-thrust coupled bearing considering thermal and pressure coupled effects. Tribol Int 180:108292. https://doi.org/10.1016/j.triboint.2023.108292
4. Zhang L, Xiong D, Su Z, Li J, Yin L, Yao Z, Zhang H (2022) Molecular dynamics simulation and experimental study of tin growth in SAC lead-free microsolder joints under thermomechanical-electrical coupling. Mater Today Commun 33:104301. https://doi.org/10.1016/j.mtcomm.2022.104301
5. Zhang P, Liu Z, Yue X, Wang P, Zhai Y (2022) Water jet impact damage mechanism and dynamic penetration energy absorption of 2A12 aluminum alloy. Vacuum 206:111532. https://doi.org/10.1016/j.vacuum.2022.111532
6. Gorji NE, O'Connor R, Brabazon D (2021) XPS and SEM characterization for powder recycling within 3d printing process. In: 24th International Conference on Material Forming (ESAFORM 2021), pp 403/1–403/9
7. Anush Raj B, Winowlin Jappes JT, Adam Khan M et al (2020) Direct metal laser sintered (DMLS) process to develop Inconel 718 alloy for turbine engine components. Optik (Stuttg) 202:163735. https://doi.org/10.1016/J.IJLEO.2019.163735
8. Delgado Camacho D, Clayton P, O'Brien WJ et al (2018) Applications of additive manufacturing in the construction industry—a forward-looking review. Autom Constr 89:110–119. https://doi.org/10.1016/J.AUTCON.2017.12.031
9. Frazier WE (2014) Metal additive manufacturing: a review. J Mater Eng Perform 23:1917–1928. https://doi.org/10.1007/S11665-014-0958-Z/FIGURES/9
10. Maleki E, Bagherifard S, Bandini M, Guagliano M (2021) Surface post-treatments for metal additive manufacturing: progress, challenges, and opportunities. Addit Manuf 37:101619. https://doi.org/10.1016/J.ADDMA.2020.101619
11. Bassoli E, Sola A, Celesti M et al (2018) Development of laser-based powder bed fusion process parameters and scanning strategy for new metal alloy grades: a holistic method formulation. Mater 11:2356. https://doi.org/10.3390/MA11122356
12. Mahmood MA, Ur Rehman A, Khraisheh M (2023) On the development of smart framework for printability maps in additive manufacturing of AISI 316L stainless steel. 3D Print Addit Manuf. https://doi.org/10.1089/3dp.2023.0016
13. Pérez-Ruiz JD, de Lacalle LNL, Urbikain G et al (2021) On the relationship between cutting forces and anisotropy features in the milling of LPBF Inconel 718 for near net shape parts. Int J Mach Tools Manuf 170:103801. https://doi.org/10.1016/J.IJMACHTOOLS.2021.103801
14. Snow Z, Nassar AR, Reutzel EW (2020) Invited review article: review of the formation and impact of flaws in powder bed fusion additive manufacturing. Addit Manuf 36:101457. https://doi.org/10.1016/J.ADDMA.2020.101457
15. Pérez-Ruiz J, González-Barrio H, Sanz-Calle M et al (2023) Machining stability improvement in LPBF printed components through stiffening by crystallographic texture control. CIRP Ann 72:141–144. https://doi.org/10.1016/J.CIRP.2023.03.025
16. Pérez-Ruiz JD, Marin F, Martínez S et al (2022) Stiffening near-net-shape functional parts of Inconel 718 LPBF considering material anisotropy and subsequent machining issues. Mech Syst Signal Process 168:108675. https://doi.org/10.1016/J.YMSSP.2021.108675
17. Liu L, Wang D, Deng G et al (2022) Laser additive manufacturing of a 316L/CuSn10 multimaterial coaxial nozzle to alleviate spattering adhesion and burning effect in directed energy deposition. J Manuf Process 82:51–63. https://doi.org/10.1016/J.JMAPRO.2022.07.038
18. Tariq U, Joy R, Wu S-H et al (2023) A state-of-the-art digital factory integrating digital twin for laser additive and subtractive manufacturing processes. Rapid Prototyp J. https://doi.org/10.1108/RPJ-03-2023-0113
19. Lu C, Gao R, Yin L, Zhang B (2023) Human-Robot Collaborative Scheduling in Energy-efficient Welding Shop. IEEE Trans Industr Inform. https://doi.org/10.1109/TII.2023.3271749
20. Fang JX, Wang JX, Wang YJ, He HT, Zhang DB, Cao Y (2022) Microstructure evolution and deformation behavior during stretching of a compositionally inhomogeneous TWIP-TRIP cantor-like alloy by laser powder deposition. Mater Sci Eng A 847:143319. https://doi.org/10.1016/j.msea.2022.143319

21. Zhang P, Wang S, Lin Z, Yue X, Gao Y, Zhang S, Yang H (2023) Investigation on the mechanism of micro-milling CoCr-FeNiAlX high entropy alloys with end milling cutters. Vacuum 211:111939. https://doi.org/10.1016/j.vacuum.2023.111939

22. Zhao Y, Jing J, Chen L, Xu F, Hou H (2021) Current research status of interface of ceramic-metal laminated composite material for armor protection. Jinshu Xuebao/Acta Metallurgica Sinica 57:1107–1125. https://doi.org/10.11900/0412.1961.2021.00051

23. Kuang W, Wang H, Li X, Zhang J, Zhou Q, Zhao Y (2018) Application of the thermodynamic extremal principle to diffusion-controlled phase transformations in Fe-C-X alloys: Modeling and applications. Acta Materialia 159:16–30. https://doi.org/10.1016/j.actamat.2018.08.008

24. Tian X, Zhao Y, Gu T, Guo Y, Xu F, Hou H (2022) Cooperative effect of strength and ductility processed by thermomechanical treatment for Cu–Al–Ni alloy. Mater Sci Eng A 849:143485. https://doi.org/10.1016/j.msea.2022.143485

25. Zhao Y, Sun Y, Hou H (2022) Core-shell structure nanoprecipitates in Fe-xCu-3.0Mn-1.5Ni-1.5Al alloys: A phase field study. Progress in Natural Science: Mater Int 32(3):358–368. https://doi.org/10.1016/j.pnsc.2022.04.001

26. Yang W, Jiang X, Tian X, Hou H, Zhao Y (2023) Phase-field simulation of nano-α′ precipitates under irradiation and dislocations. J Mater Res Technol 22:1307–1321. https://doi.org/10.1016/j.jmrt.2022.11.165

27. Guo Q, Hou H, Pan Y, Pei X, Song Z, Liaw PK, Zhao Y (2023) Hardening-softening of Al0.3CoCrFeNi high-entropy alloy under nanoindentation. Mater Des 231:112050. https://doi.org/10.1016/j.matdes.2023.112050

28. Wang J, Pan Z, Wang Y, Wang L, Su L, Cuiuri D, Li H (2020) Evolution of crystallographic orientation, precipitation, phase transformation and mechanical properties realized by enhancing deposition current for dual-wire arc additive manufactured Ni-rich NiTi alloy. Addit Manuf 34:101240. https://doi.org/10.1016/j.addma.2020.101240

29. Zhao P, Zhu J, Li M, Shao G, Lu H, Wang H, He J (2023) Theoretical and experimental investigations on the phase stability and fabrication of high-entropy monoborides. J Eur Ceram Soc 43(6):2320–2330. https://doi.org/10.1016/j.jeurceramsoc.2023.01.026

30. Wang K, Zhu J, Wang H, Yang K, Zhu Y, Qing Y, He J (2022) Air plasma-sprayed high-entropy (Y0.2Yb0.2Lu0.2Eu0.2Er0.2)3Al5O12 coating with high thermal protection performance. J Adv Ceram 11(10):1571–1582. https://doi.org/10.1007/s40145-022-0630-2

31. Cooke S, Ahmadi K, Willerth S, Herring R (2020) Metal additive manufacturing: technology, metallurgy and modelling. J Manuf Process 57:978–1003. https://doi.org/10.1016/J.JMAPRO.2020.07.025

32. Bartlett JL, Li X (2019) An overview of residual stresses in metal powder bed fusion. Addit Manuf 27:131–149. https://doi.org/10.1016/J.ADDMA.2019.02.020

33. Wang J, Zhu R, Liu Y, Zhang L (2023) Understanding melt pool characteristics in laser powder bed fusion: an overview of single- and multi-track melt pools for process optimization. Adv Powder Mater 2:100137. https://doi.org/10.1016/J.APMATE.2023.100137

34. Everton S, Dickens P, Tuck C, Dutton B (2018) Using laser ultrasound to detect subsurface defects in metal laser powder bed fusion components. JOM 70:378–383. https://doi.org/10.1007/S11837-017-2661-7/FIGURES/3

35. Cerniglia D, Scafidi M, Pantano A, Rudlin J (2015) Inspection of additive-manufactured layered components. Ultrasonics 62:292–298. https://doi.org/10.1016/J.ULTRAS.2015.06.001

36. Brennan MC, Keist JS, Palmer TA et al (2021) Defects in metal additive manufacturing processes. J Mater Eng Perform 30:4808–4818. https://doi.org/10.1007/S11665-021-05919-6

37. Blecher JJ, Palmer TA, Debroy T (2016) Porosity in Thick Section Alloy 690 Welds – Experiments, Modeling, Mechanism, and Remedy Analyzing the characteristics of laser and hybrid laser-gas metal arc welded Alloy 690 with a compositionally identical filler metal. Welding J 95:17-s–26-s

38. Trevisan RE, Schwemmer DD, Olson DL (1990) The Fundamentals of Weld Metal Pore Formation. Mater Process: Theory Pract 8:79–115. https://doi.org/10.1016/B978-0-444-87427-6.50009-5

39. Everton SK, Hirsch M, Stavroulakis PI et al (2016) Review of in-situ process monitoring and in-situ metrology for metal additive manufacturing. Mater Des 95:431–445. https://doi.org/10.1016/J.MATDES.2016.01.099

40. Cross CE (2005) On the origin of weld solidification cracking. In: Hot cracking phenomena in welds. Springer Berlin Heidelberg, Berlin, Heidelberg, pp 3–18. https://doi.org/10.1007/3-540-27460-X_1/COVER

41. Lippold JC, Kotecki DJ (2005) Welding Metallurgy and Weldability of Stainless Steels, p 376. Wiley-VCH

42. Shiva S, Palani IA, Mishra SK et al (2015) Investigations on the influence of composition in the development of Ni–Ti shape memory alloy using laser based additive manufacturing. Opt Laser Technol 69:44–51. https://doi.org/10.1016/J.OPTLASTEC.2014.12.014

43. Gusarov AV, Pavlov M, Smurov I (2011) Residual stresses at laser surface remelting and additive manufacturing. Phys Procedia 12:248–254. https://doi.org/10.1016/J.PHPRO.2011.03.032

44. Dinda GP, Song L, Mazumder J (2008) Fabrication of Ti-6Al-4V scaffolds by direct metal deposition. Metall Mater Trans A Phys Metall Mater Sci 39:2914–2922. https://doi.org/10.1007/S11661-008-9634-Y/FIGURES/11

45. Öztürk N, Yildiz AR, Kaya N, Öztürk F (2006) Neuro-Genetic Design Optimization Framework to Support the Integrated Robust Design Optimization Process in CE. Concurr Eng 14:5–16. https://doi.org/10.1177/1063293X06063314

46. Gao S, Li H, Huang H, Kang R (2022) Grinding and lapping induced surface integrity of silicon wafers and its effect on chemical mechanical polishing. Appl Surf Sci 599:153982. https://doi.org/10.1016/j.apsusc.2022.153982

47. Xie B, Li H, Ning Y, Fu M (2023) Discontinuous dynamic recrystallization and nucleation mechanisms associated with 2-, 3- and 4-grain junctions of polycrystalline nickel-based superalloys. Mater Des 231:112041. https://doi.org/10.1016/j.matdes.2023.112041

48. Zhang H, Xiao Y, Xu Z, Yang M, Zhang L, Yin L, Cai X (2022) Effects of Ni-decorated reduced graphene oxide nanosheets on the microstructural evolution and mechanical properties of Sn-3.0Ag-0.5Cu composite solders. Intermetallics 150:107683. https://doi.org/10.1016/j.intermet.2022.107683

49. Chen Y, Sun S, Zhang T, Zhou X, Li S (2020) Effects of postweld heat treatment on the microstructure and mechanical properties of laser-welded NiTi/304SS joint with Ni filler. Mater Sci Eng A 771:138545. https://doi.org/10.1016/j.msea.2019.138545

50. Yuhua C, Yuqing M, Weiwei L, Peng H (2017) Investigation of welding crack in micro laser welded NiTiNb shape memory alloy and Ti6Al4V alloy dissimilar metals joints. Opt Laser Technol 91:197–202. https://doi.org/10.1016/j.optlastec.2016.12.028

51. Guo K, Gou G, Lv H, Shan M (2022) Jointing of CFRP/5083 aluminum alloy by induction brazing: Processing, connecting mechanism, and fatigue performance. Coatings 12(10):1559. https://doi.org/10.3390/coatings12101559

52. Yildiz AR, Öztürk N, Kaya N, Öztürk F (2003) Integrated optimal topology design and shape optimization using neural networks. Struct Multidiscip Optim 25:251–260. https://doi.org/10.1007/S00158-003-0300-0/METRICS

53. Fu ZH, Yang BJ, Shan ML, Li T, Zhu ZY, Ma CP, Gao W (2020) Hydrogen embrittlement behavior of SUS301L-MT stainless

steel laser-arc hybrid welded joint localized zones. Corros Sci 164:108337. https://doi.org/10.1016/j.corsci.2019.108337

54. Zhu ZY, Liu YL, Gou GQ, Gao W, Chen J (2021) Effect of heat input on interfacial characterization of the butter joint of hot-rolling CP-Ti/Q235 bimetallic sheets by Laser + CMT. Scientific Reports 11(1):10020. https://doi.org/10.1038/s41598-021-89343-9

55. Zhu Q, Chen J, Gou G, Chen H, Li P (2017) Ameliorated longitudinal critically refracted—Attenuation velocity method for welding residual stress measurement. J Mater Process Technol 246:267–275. https://doi.org/10.1016/j.jmatprotec.2017.03.022

56. Liao D, Zhu S, Keshtegar B, Qian G, Wang Q (2020) Probabilistic framework for fatigue life assessment of notched components under size effects. Int J Mech Sci 181:105685. https://doi.org/10.1016/j.ijmecsci.2020.105685

57. Niu X, Zhu S, He J, Liao D, Correia JAFO, Berto F, Wang Q (2022) Defect tolerant fatigue assessment of AM materials: Size effect and probabilistic prospects. Int J Fatigue 160:106884. https://doi.org/10.1016/j.ijfatigue.2022.106884

58. Li X, Zhu S, Liao D, Correia JAFO, Berto F, Wang Q (2022) Probabilistic fatigue modelling of metallic materials under notch and size effect using the weakest link theory. Int J Fatigue 159:106788. https://doi.org/10.1016/j.ijfatigue.2022.106788

59. Meng Z, Qian Q, Xu M et al (2023) PINN-FORM: a new physics-informed neural network for reliability analysis with partial differential equation. Comput Methods Appl Mech Eng 414:116172. https://doi.org/10.1016/J.CMA.2023.116172

60. Aye CM, Pholdee N, Yildiz AR et al (2019) Multi-surrogate-assisted metaheuristics for crashworthiness optimisation. Int J Veh Des 80:223–240. https://doi.org/10.1504/IJVD.2019.109866

61. Aslan B, Yildiz AR (2020) Optimum design of automobile components using lattice structures for additive manufacturing. Mater Test 62:633–639. https://doi.org/10.3139/120.111527/MACHINEREADABLECITATION/RIS

62. Günaydln AC, Ylldlz AR, Kaya N (2022) Multi-objective optimization of build orientation considering support structure volume and build time in laser powder bed fusion. Mater Test 64:323–338. https://doi.org/10.1515/MT-2021-2075/MACHINEREADABLECITATION/RIS

63. Tariq U, Joy R, Wu SH et al (2023) A state-of-the-art digital factory integrating digital twin for laser additive and subtractive manufacturing processes. Rapid Prototyp J. https://doi.org/10.1108/RPJ-03-2023-0113/FULL/XML

64. Ye D, Hong GS, Zhang Y et al (2018) Defect detection in selective laser melting technology by acoustic signals with deep belief networks. Int J Adv Manuf Technol 96:2791–2801. https://doi.org/10.1007/S00170-018-1728-0/METRICS

65. Shevchik SA, Kenel C, Leinenbach C, Wasmer K (2018) Acoustic emission for in situ quality monitoring in additive manufacturing using spectral convolutional neural networks. Addit Manuf 21:598–604. https://doi.org/10.1016/J.ADDMA.2017.11.012

66. Zhang Y, Hong GS, Ye D et al (2018) Extraction and evaluation of melt pool, plume and spatter information for powder-bed fusion AM process monitoring. Mater Des 156:458–469. https://doi.org/10.1016/J.MATDES.2018.07.002

67. Grasso M, Demir AG, Previtali B, Colosimo BM (2018) In situ monitoring of selective laser melting of zinc powder via infrared imaging of the process plume. Robot Comput Integr Manuf 49:229–239. https://doi.org/10.1016/J.RCIM.2017.07.001

68. Scime L, Beuth J (2019) Using machine learning to identify in-situ melt pool signatures indicative of flaw formation in a laser powder bed fusion additive manufacturing process. Addit Manuf 25:151–165. https://doi.org/10.1016/J.ADDMA.2018.11.010

69. Gobert C, Reutzel EW, Petrich J et al (2018) Application of supervised machine learning for defect detection during metallic powder bed fusion additive manufacturing using high resolution

imaging. Addit Manuf 21:517–528. https://doi.org/10.1016/J.ADDMA.2018.04.005

70. Ye D, Hsi Fuh JY, Zhang Y et al (2018) In situ monitoring of selective laser melting using plume and spatter signatures by deep belief networks. ISA Trans 81:96–104. https://doi.org/10.1016/J.ISATRA.2018.07.021

71. Kwon O, Kim HG, Ham MJ et al (2020) A deep neural network for classification of melt-pool images in metal additive manufacturing. J Intell Manuf 31:375–386. https://doi.org/10.1007/S10845-018-1451-6/FIGURES/9

72. Okaro IA, Jayasinghe S, Sutcliffe C et al (2018) Automatic Fault Detection for Selective Laser Melting Using Semi-Supervised Machine Learning. https://doi.org/10.20944/PREPRINTS201809.0346.V1

73. Okaro IA, Jayasinghe S, Sutcliffe C et al (2019) Automatic fault detection for laser powder-bed fusion using semi-supervised machine learning. Addit Manuf 27:42–53. https://doi.org/10.1016/J.ADDMA.2019.01.006

74. Grasso M, Laguzza V, Semeraro Q, Colosimo BM (2017) In-process monitoring of selective laser melting: spatial detection of defects via image data analysis. J Manuf Sci Eng Trans ASME 139:051001. https://doi.org/10.1115/1.4034715/377587

75. Zur Jacobsmuhlen J, Kleszczynski S, Witt G, Merhof D (2015) Detection of elevated regions in surface images from laser beam melting processes. In: IECON 2015 - 41st Annu Conf IEEE Ind Electron Soc, pp 1270–1275. https://doi.org/10.1109/IECON.2015.7392275

76. Caggiano A, Zhang J, Alfieri V et al (2019) Machine learning-based image processing for on-line defect recognition in additive manufacturing. CIRP Ann 68:451–454. https://doi.org/10.1016/J.CIRP.2019.03.021

77. Jafari-Marandi R, Khanzadeh M, Tian W et al (2019) From in-situ monitoring toward high-throughput process control: cost-driven decision-making framework for laser-based additive manufacturing. J Manuf Syst 51:29–41. https://doi.org/10.1016/J.JMSY.2019.02.005

78. Khanzadeh M, Chowdhury S, Tschopp MA et al (2018) In-situ monitoring of melt pool images for porosity prediction in directed energy deposition processes. IISE Transactions 51(5):437–455. https://doi.org/10.1080/24725854.2017.1417656

79. Mahmood MA, Visan AI, Ristoscu C, Mihailescu IN (2021) Artificial Neural Network Algorithms for 3D Printing. Materials 14(1):163

80. Zhao L, Yue H, Guo C et al (2020) Analytical modelling and experimental study of the cladding characteristics of a laser powder-fed additive manufacturing process. Int J Adv Manuf Technol 109:2891–2900. https://doi.org/10.1007/s00170-020-05813-w

81. Zhang Z, Huang Y, Rani Kasinathan A et al (2019) 3-Dimensional heat transfer modeling for laser powder-bed fusion additive manufacturing with volumetric heat sources based on varied thermal conductivity and absorptivity. Opt Laser Technol 109:297–312. https://doi.org/10.1016/J.OPTLASTEC.2018.08.012

82. Johnson L, Mahmoudi M, Zhang B et al (2019) Assessing printability maps in additive manufacturing of metal alloys. Acta Mater 176:199–210. https://doi.org/10.1016/j.actamat.2019.07.005

83. He P, Sun C, Wang Y (2021) Material distortion in laser-based additive manufacturing of fuel cell component: three-dimensional numerical analysis. Addit Manuf 46:102188. https://doi.org/10.1016/j.addma.2021.102188

84. Ahn DG, Byun KW, Kang MC (2010) Thermal characteristics in the cutting of Inconel 718 superalloy using CW Nd:YAG laser. J Mater Sci Technol 26:362–366. https://doi.org/10.1016/S1005-0302(10)60059-X

85. García Navas V, Arriola I, Gonzalo O, Leunda J (2013) Mechanisms involved in the improvement of Inconel 718 machinability by laser

assisted machining (LAM). Int J Mach Tools Manuf 74:19–28. https://doi.org/10.1016/J.IJMACHTOOLS.2013.06.009

86. Ziebland H, Burton JTA (1958) The thermal conductivity of nitrogen and argon in the liquid and gaseous states. Br J Appl Phys 9:52. https://doi.org/10.1088/0508-3443/9/2/302

87. Aggarangsi P, Beuth JL (2006) Localized Preheating Approaches for Reducing Residual Stress in Additive Manufacturing. In: International Solid Freeform Fabrication Symposium, Austin Texas, pp 709–720

88. Heigel JC, Michaleris P, Reutzel EW (2015) Thermo-mechanical model development and validation of directed energy deposition additive manufacturing of Ti–6Al–4V. Addit Manuf 5:9–19. https://doi.org/10.1016/J.ADDMA.2014.10.003

89. Pottlacher G, Hosaeus H, Kaschnitz E, Seifter A (2002) Thermophysical properties of solid and liquid Inconel 718 alloy. Scand J Metall 31:161–168. https://doi.org/10.1034/j.1600-0692.2002.310301.x

90. Le TN, Lo YL, Lin ZH (2020) Numerical simulation and experimental validation of melting and solidification process in selective laser melting of IN718 alloy. Addit Manuf 36:101519. https://doi.org/10.1016/j.addma.2020.101519

91. Tongtai Tongtai-AM250. https://www.tongtai.com.tw/en/product-detail.php?id=314

92. Sood AK, Ohdar RK, Mahapatra SS (2012) Experimental investigation and empirical modelling of FDM process for compressive strength improvement. J Adv Res 3:81–90. https://doi.org/10.1016/j.jare.2011.05.001

93. Sood AK, Equbal A, Toppo V et al (2012) An investigation on sliding wear of FDM built parts. CIRP J Manuf Sci Technol 5:48–54. https://doi.org/10.1016/j.cirpj.2011.08.003

94. Mukherjee T, Zuback JS, De A, DebRoy T (2016) Printability of alloys for additive manufacturing. Sci Rep 6:1–8. https://doi.org/10.1038/srep19717

95. Carroll BE, Palmer TA, Beese AM (2015) Anisotropic tensile behavior of Ti–6Al–4V components fabricated with directed energy deposition additive manufacturing. Acta Mater 87:309–320. https://doi.org/10.1016/J.ACTAMAT.2014.12.054

96. King WE, Barth HD, Castillo VM et al (2014) Observation of keyhole-mode laser melting in laser powder-bed fusion additive manufacturing. J Mater Process Technol 214:2915–2925. https://doi.org/10.1016/j.jmatprotec.2014.06.005

97. Roehling JD, Perron A, Fattebert JL et al (2018) Rapid solidification in bulk Ti-Nb alloys by single-track laser melting. JOM 70:1589–1597. https://doi.org/10.1007/S11837-018-2920-2/FIGURES/4

98. Seede R, Shoukr D, Zhang B et al (2020) An ultra-high strength martensitic steel fabricated using selective laser melting additive manufacturing: densification, microstructure, and mechanical properties. Acta Mater 186:199–214. https://doi.org/10.1016/j.actamat.2019.12.037

99. Kamath C, El-Dasher B, Gallegos GF, King WE, Sisto A (2014) Density of additively-manufactured, 316L SS parts using laser powder-bed fusion at powers up to 400 W. Int J Adv Manuf Technol 74:65–78. https://doi.org/10.1007/S00170-014-5954-9

100. Zheng T, Pan S, Murali N et al (2022) Selective laser melting of novel 7075 aluminum powders with internally dispersed TiC nanoparticles. Mater Lett 319:132268. https://doi.org/10.1016/J.MATLET.2022.132268

101. Pan SH, Yao GC, Cui YN et al (2022) Additive manufacturing of tungsten, tungsten-based alloys, and tungsten matrix composites. Tungsten 5:1–31. https://doi.org/10.1007/S42864-022-00153-6

102. Wang S, Ning J, Zhu L et al (2022) Role of porosity defects in metal 3D printing: formation mechanisms, impacts on properties and mitigation strategies. Mater Today 59:133–160. https://doi.org/10.1016/J.MATTOD.2022.08.014

103. Lack of fusion. BOConline UK

104. Rehman AU, Pitir F, Salamci MU (2021) Laser powder bed fusion (LPBF) of In718 and the impact of pre-heating at 500 and 1000 °C: Operando Study. Mater 14:6683. https://doi.org/10.3390/MA14216683

105. Chen Q, Zhao Y, Strayer S et al (2021) Elucidating the effect of preheating temperature on melt pool morphology variation in Inconel 718 laser powder bed fusion via simulation and experiment. Addit Manuf 37:101642. https://doi.org/10.1016/J.ADDMA.2020.101642

106. Tan P, Kiran R, Zhou K (2021) Effects of sub-atmospheric pressure on keyhole dynamics and porosity in products fabricated by selective laser melting. J Manuf Process 64:816–827. https://doi.org/10.1016/J.JMAPRO.2021.01.058

107. Yuan W, Chen H, Li S et al (2022) Understanding of adopting flat-top laser in laser powder bed fusion processed Inconel 718 alloy: simulation of single-track scanning and experiment. J Mater Res Technol 16:1388–1401. https://doi.org/10.1016/j.jmrt.2021.12.077

108. Wang HY, Lo YL, Tran HC et al (2021) Systematic approach for reducing micro-crack formation in Inconel 713LC components fabricated by laser powder bed fusion. Rapid Prototyp J 27:1548–1561. https://doi.org/10.1108/RPJ-11-2020-0282/FULL/XML

109. Sokoluk M, Yuan J, Pan S, Li X (2021) Nanoparticles enabled mechanism for hot cracking elimination in aluminum alloys. Metall Mater Trans A Phys Metall Mater Sci 52:3083–3096. https://doi.org/10.1007/S11661-021-06302-9/FIGURES/12

110. Sokoluk M, Cao C, Pan S, Li X (2019) Nanoparticle-enabled phase control for arc welding of unweldable aluminum alloy 7075. Nat Commun 10:98. https://doi.org/10.1038/s41467-018-07989-y

111. Martin JH, Yahata BD, Hundley JM et al (2017) 3D printing of high-strength aluminium alloys. Nat 549:365–369. https://doi.org/10.1038/nature23894

112. Pardi T, Krzywdzinski M, Luethje B (2020) Digital manufacturing revolutions as political projects and hypes: Evidences from the auto sector, ILO Working Paper 3 (Geneva, ILO)